Monthly Notices
of the
ROYAL ASTRONOMICAL SOCIETY

MNRAS **497,** 1475–1487 (2020)
Advance Access publication 2020 July 20

doi:10.1093/mnras/staa2091

Structure of accretion flows in the nova-like cataclysmic variable RW Tri

G. Subebekova,[1] S. Zharikov ,[2]★ G. Tovmassian,[2] V. Neustroev ,[3] M. Wolf ,[4] M.-S. Hernandez,[5] H. Kučáková[4,6,7] and S. Khokhlov[1]

[1]*Al-Farabi Kazakh National University, Al-Farabi Ave., 71, 050040 Almaty, Kazakhstan*
[2]*Instituto de Astronomía, Universidad Nacional Autónoma de México, Apdo. Postal 877, Ensenada, 22800 Baja California, México*
[3]*Space Physics and Astronomy research unit, University of Oulu, PO Box 3000, FIN-90014 Oulu, Finland*
[4]*Astronomical Institute, Faculty of Mathematics and Physics, Charles University, V Holešovičkách 2, CZ-180 00 Praha 8, Czech Republic*
[5]*Instituto de Física y Astronomía, Universidad de Valparaíso, Av. Gran Bretaña, 1111 Valparaíso, Chile*
[6]*Astronomical Institute, Academy of Sciences, Fričova 298, CZ-251 65, Czech Republic*
[7]*Research Centre for Theoretical Physics and Astrophysics, Institute of Physics, Silesian University in Opava, Bezručovo nám. 13, CZ-746 01 Opava, Czech Republic*

Accepted 2020 July 9. Received 2020 July 9; in original form 2020 May 20

ABSTRACT

We obtained photometric observations of the nova-like (NL) cataclysmic variable RW Tri and gathered all available AAVSO and other data from the literature. We determined the system parameters and found their uncertainties using the code developed by us to model the light curves of binary systems. New time-resolved optical spectroscopic observations of RW Tri were also obtained to study the properties of emission features produced by the system. The usual interpretation of the single-peaked emission lines in NL systems is related to the bi-conical wind from the accretion disc's inner part. However, we found that the Hα emission profile is comprised of two components with different widths. We argue that the narrow component originates from the irradiated surface of the secondary, while the broader component's source is an extended, low-velocity region in the outskirts of the accretion disc, located opposite to the collision point of the accretion stream and the disc. It appears to be a common feature for long-period NL systems – a point we discuss.

Key words: binaries: spectroscopic – stars: individual: RW Tri – novae, cataclysmic variables.

1 INTRODUCTION

Cataclysmic variables (CVs) are interacting binaries comprised of a white dwarf (WD) as the primary and a late-type (K-M type) main-sequence star or a brown dwarf as the secondary (Warner 1995). The secondary star fills its Roche lobe and looses matter via the inner Lagrangian point L_1 forming an accretion disc around the WD, if the magnetic field of the WD is not strong enough to prevent this. CVs which show outbursting behaviour related to an explosive transition in the disc between low- and high-temperature/density states are called dwarf novae (DNe). In contrast to them, there are systems at the long-period end of the orbital period distribution of CVs ($P_{\rm orb} >$ 3 h), which exhibit a high-accretion rate $\geq 10^{-9}\,{\rm M}_{\odot}$. Such systems are called nova-likes (NLs); their accretion discs stay in a high state most of the time. Low-resolution optical spectra of NLs show a blue continuum with single-peaked Balmer emission lines, even for high-inclination eclipsing systems. In some cases, the emission lines are flanked by absorption features. The ultraviolet (UV) spectrum of NLs is dominated by emission from the accretion disc. They show resonance lines such as N V, Si IV, and C IV often having P Cygni-like and/or blueshifted absorption profiles (Noebauer et al. 2010, and references therein). Several models (Stark broadening – Lin, Williams & Stover 1988; magnetic accretion – Williams 1989; disc-overflow accretion – Hellier & Robinson 1994; an extended bright spot as the dominant source of emission lines – Dhillon, Marsh & Jones 1997; Tovmassian et al. 2014; and wind emission – Honeycutt, Schlegel & Kaitchuck 1986; Murray & Chiang 1996; Noebauer et al. 2010; Puebla et al. 2011; Matthews et al. 2015 have been suggested to explain NLs characteristics. The wind model which is more developed than others is able to reproduce hydrogen and and helium recombination lines in the UV spectra of NLs, as well as a recombination continuum bluewards of the Balmer edge. But, the model produces stronger-than-observed He II lines in the optical region and too much of a collisionally exciting contribution to the UV resonance lines. It was reported that single-peaked profiles of Blamer lines in NLs probably have complex structure (Horne, Lanning & Gomer 1982; Kaitchuck, Honeycutt & Schlegel 1983; Mauche et al. 1994; Thoroughgood et al. 2004). Recent high-resolution spectral study of two NL systems (Hernandez et al. 2017) demonstrates that Balmer emission-line profiles can be divided into two components arising from two distinct regions. The source of the narrow, low-velocity component is the irradiated face of the secondary star. The wide component, according to Hernandez et al. (2017), is emanated from an outflow region in the vicinity of the L_3 point.

To verify this idea, we obtained new, time-resolved, high-resolution optical spectroscopic observations of RW Tri – a well-studied NL system. Results of our spectroscopy combined with the new photometric data allowed us to redefine the system parameters of RW Tri by using light-curve modelling tool (Zharikov et al. 2013) and obtain additional evidence in favour of this hypothesis.

★ E-mail: zhar@astrosen.unam.mx

Table 1. Estimations of RW Tri system parameters.

Reference	Distance (pc)	i (^{o})	M_1 ($M_\odot$)	M_2 ($M_\odot$)	R_2 ($R_\odot$)	SpT_2	R^{out}_{disc} ($R_\odot$)
Longmore et al. (1981)	400	>80	1.4–2.0	0.7	0.7–0.8	K5V	0.7–0.8
Frank & King (1981)	180(70)	82	1.3(0.7)	0.47	$0.56^{+0.06}_{-0.02}$	M0V	0.76–0.94
Kaitchuck et al. (1983)	–	67–75	0.64(1)	0.76(2)	–	K5–K7	0.34(12)[a]
Kaitchuck et al. (1983)	–	67–75	0.54(9)	0.69(2)	–	K5–K7	0.22(5)[a]
Rutten, van Paradijs & Tinbergen (1992)	–	75	0.7	0.6	–	–	0.25[a]
Smak (1995)	240(40)	70.5	0.45(15)	0.63(15)	–	–	0.25
Poole et al. (2003)	–	–	0.4–0.7	0.3–0.4	–	–	–
Smak (2019)	–	72.5(2.5)	0.6(2)	0.48(15)	–	–	–

Notes. SpT_2 is the spectral type of the secondary. [a]Optical radius of the accretion disc.

This paper is structured as follows. In Section 2, we describe previous progress in the study of RW Tri. Our spectroscopic observations of RW Tri, the photometric data, and the corresponding data reduction are given in Section 3. The photometric monitoring of RW Tri, the optical light-curve modelling, and the system parameters estimation is presented in Section 4. In Section 5, we analyse RW Tri spectra and behaviours of its emission lines. The general discussion of the results and their application to NLs placed in a similar orbital period range are given in Section 6. Our conclusions are presented in Section 7.

2 RW TRIANGULI

RW Tri was discovered as an eclipsing binary system by Protitch (1938). *GAIA* distance of the system is 315.5 ± 5.0 pc (Luri et al. 2018). It is in a good agreement with the previous *Hubble Space Telescope (HST)* parallax measurements 341^{-31}_{+38} pc (McArthur et al. 1999). The first extensive photoelectric photometry in the *UBV* system was reported by Walker (1963). He showed that the object besides eclipses varies in brightness at a long and short time-scale. The depth of eclipse depends on the brightness of the system, which itself does not present any periodicity either on long or short scales. The orbital period of the system is $P_{orb} = 0.231\,883\,24 \pm 4 \times 10^{-8}$ d (Africano et al. 1978). The light curve of RW Tri has a close similarity to UX UMa, a prototype of NLs. Longmore et al. (1981) observed RW Tri at the near-infrared (NIR) *JHK* bands. The NIR light curves showed a deep primary minimum whose depth decreases towards longer wavelengths, and a shallow secondary minimum, not seen at the optical wavelengths. Light curves allowed to estimate basic system parameters listed in Table 1. Frank & King (1981) used infrared and visual light curves of RW Tri during quiescence to fit simultaneously by a model in which a red dwarf eclipses an optically thick steady-state accretion disc. They obtained self-consistent system parameters for their model, also included in Table 1. Kaitchuck et al. (1983) conducted time-resolved spectrophotometry of RW Tri to study the rapid evolution of the emission-line spectrum as the accretion disc undergoes occultation by the secondary star. The object was in a dim state at $B \approx 13.3$ mag. Kaitchuck et al. (1983) found that profiles of Balmer lines show a double component structure. The line profiles presented in the form of trailed spectra (see fig. 8–10 by Kaitchuck et al. 1983) leave an impression of the presence of two anti-phased components that cross at phase φ =0.5 and 0.0. Horne & Stiening (1985) reported simultaneous high-speed *UBR*-photometry of RW Tri and the study of its accretion disc based on eclipse mapping. They propose that the disc is optically thick, with temperature ranging from 10 000 K at the outer edge to 40 000 K near the centre. The radial temperature profile is consistent with the expected $T \propto R^{-3/4}$ law for steady-state accretion.

Robinson, Shetrone & Africano (1991) revised the eclipse ephemeris and estimated the limit of the period rate change $\dot{P} < 5.6 \times 10^{-12}$. They also re-evaluated an upper limit of the mass transfer rate to $\dot{M} < 5.6 \times 10^{-9}$ $M_\odot$ yr^{-1}. Rutten & Dhillon (1992) presented phase-resolved spectropolarimetric observations of RW Tri and did not find any intrinsic linear polarization to the binary system. They also concluded that a significant fraction of line emission is radiated from a source other than the accretion disc.

The first Doppler tomography in Hβ, He I λ4471 Å, and He II λ4686 Å of RW Tri were presented by Kaitchuck et al. (1994).

Still, Dhillon & Jones (1995) carried out time-resolved spectrophotometry of RW Tri intending to define the regions of optical emission. They found that the variation of the Balmer line profile can be interpreted as a two-component emission. There is no evidence of an eclipse in the emission wings of these lines at phase zero, and there is no suggestion of a rotational disturbance in either the broad emission component or the absorption wings, expected from a rotating accretion disc.

RW Tri was observed with the Goddard High-Resolution Spectrograph (GHRS) with the *HST* in a program primarily designed to study accretion disc winds (Mason, Drew & Knigge 1997). The light curve of the object exhibits a prominent UV eclipse. It is U-shaped and relatively wide (full width at half-light, $\Delta\varphi_{0.5} = 0.07$ cycles). The most interesting feature of the reported UV light curve is a dip in the UV flux during the half-cycle preceding the eclipse. The dip shows the maximum depth at the phase $\varphi \approx 0.7$. It has a distinct saw-tooth shape with a rapid fall beginning at phase of $\varphi \sim 0.5-0.6$ and a more gradual rise, which is not complete until the phase of $\varphi \sim 0.2$ (i.e. post-eclipse).

The secondary in RW Tri is probably M-type main-sequence star judging from the *I*- and *K*-band spectroscopy (Dhillon et al. 2000; Poole et al. 2003). The *K*-band light curve reaches $K = 12.17$ at the primary minimum (Longmore et al. 1981), which combined with the distance results in $M_{K_s} \geq 4.65$. It limits the spectral class of the secondary to later than K6V or $T_2 \leq 4250$ K. However, much deeper eclipse to $V = 16.23 \pm 0.07$ establishes the upper limit to $M_V \geq 8.47$ or $T_2 \leq 4000$ K (Pecaut & Mamajek 2013). Poole et al. (2003) made an effort to determine the orbital velocity of the secondary using time-resolved spectroscopy in *I* and *K* bands by skew-mapping and cross-correlation techniques. They found a radial velocity amplitude of 250 ± 47 km s^{-1} in the *I* band, and 229 ± 29km s^{-1} in the *K* band. A combination of these results leads to the best estimations of the primary and the secondary stellar masses in the range of 0.4–0.7 and 0.3–0.4 $M_\odot$, respectively. The last determination of the system

Table 2. Log of spectral observations of RW Tri.

Date (DD/MM/YYYY)	HJD start + 2450000	Number of exp.	Exp. time (s)	Duration (h)
08/09/2016	7639.8046	15	1200	4.9
09/09/2016	7640.7895	16	1200	5.2
10/09/2016	7641.7732	17	1200	5.7
11/09/2016	7642.7726	17	1200	5.6
12/09/2016	7643.7624	14	1200	4.6
27/09/2016	7658.9281[a]	6	240	0.4
14/10/2017	8040.9466[a]	6	900	1.5

Notes. Spectra were obtained with the OAN SPM REOSC Echelle spectrograph for which B&Ch spectrograph was used. [a]Spectra that were not obtained with the OAN SPM REOSC echelle spectrograph for which B&Ch spectrograph was used.

parameters was reported by Smak (2019) based on new spectroscopic results and old photometric data where negative superhumps were detected.

In Table 1, we summarize the results of system parameters determination in previous studies of RW Tri. As can be seen, despite a large amount of data and many carried out studies, there is a significant spread of the determined parameter values. This encouraged us to attempt to refine them using the light-curve modelling technique developed by us.

3 OBSERVATIONS AND DATA REDUCTION

A time-resolved CCD photometry of RW Tri has been obtained at the Ondřejov Observatory, Czech Republic, since 2012. The Mayer 0.65 m (*f*/3.6) reflecting telescope with the CCD camera G2-3200 and *VR* photometric filters were used. APHOT, synthetic aperture photometry, and astrometry software were used for data reduction. Differential photometry was performed using suitable comparison stars, and a heliocentric correction was applied. Computers at the telescope are synchronized using a time-server provided by `tick.usno.navy.mil` every 2 min. These corrections are usually of the order of 10^{-3} s.

In addition, time-resolved *V*-band CCD photometric data were obtained on 2016 September 8–11, and on 2016 November 14, 16, and 17 using the 0.84-m telescope and MEXMAN filter-wheel of Observatorio Astronomico Nacional at San Pedro Mártir (OAN-SPM), Mexico.

The spectroscopic data of RW Tri were obtained using the Echelle REOSC spectrograph (Levine & Chakarabarty 1995) and Boller and Chivens long-slit spectrograph attached to the 2.1-m telescope of the OAN-SPM. The Echelle spectrograph provides spectra spread over 27 orders, covering the spectral range 3500–7100 Å with the spectral resolving power of $R = 18000$. A total of 79 Echelle spectra were obtained in 2016, September, and October. The Echelle spectroscopy was obtained simultaneously with time-resolved photometric observations.

Also, a number of low-resolution spectra were obtained using Boller and Chivens long-slit spectrograph. The Boller and Chivens cover spectral range 3900–7400 Å with the spectral resolving power of $R \approx 2000$. All spectroscopic observations were obtained under photometric conditions. Standard procedures, including bias and flat-field correction, cosmic ray removal, and wavelength calibration, were applied. The log of spectroscopic observations is presented in Table 2.

4 PHOTOMETRY AND THE LIGHT-CURVE MODELLING OF RW TRI

A fragment of about a one-month-long *V*-band light curve of RW Tri based on the AAVSO data is plotted in Fig. 1. Besides eclipses, the object shows long-term variability in a 12.8–13.7 range of magnitudes. A zoom on one orbital period is presented at the bottom left-hand panel, on two different occasions (overplotted), when the flickering is present (open circles) and when it is absent (filled circles; the light curve per period is repeated twice). The flickering appears and disappears randomly. The eclipse depth (ΔV) depends on the underlying brightness (V) of the object (see the bottom right-hand panel of Fig. 1). All these features are generally well known (see Section 1), but the deduced system parameters demonstrate a large spread (see Table 1).

We used gathered photometric observations to analyse eclipse light curves using a tool developed by Zharikov et al. (2013) to improve the system's definition. Briefly, the model includes a primary WD, a secondary red dwarf star, a stream of accretion matter, thick $h(r) = h(r_{\rm out})(r/r_{\rm out})^{\gamma}$ ($\gamma = 1$) accretion disc, and an extended hotspot/line. The WD is a sphere, defined by the mass–radii relation in (2.83b Warner 1995). The secondary is assumed to fill its Roche lobe, and the Roche lobe shape is directly calculated using equation (2.2 Warner 1995) for equipotential $\Phi(L_1)$. The surface of each component of the system is divided into a series of triangles. We assume that each triangle emits as a blackbody with the corresponding temperature. The limb darkening (Claret, Hauschildt & Witte 2012) and the illumination of the secondary by the primary are also included. Each element's intensity is convolved with the corresponding filter bandpass and converted into the flux taking into account the element surface, orientation, distance to the system, and interstellar absorption. The light curves of individual components and the binary system as a whole were obtained by integrating the emission from all the elements lying in view. Details of the light-curve modelling of similar NLs are described in Tovmassian et al. (2014) and Hernandez et al. (2017).

After revising a large volume of the AAVSO data, and our proper observations, we selected examples of two different eclipses of RW Tri presented in the upper right-hand corner of Fig. 2. However, we note that these two extreme examples represent typical eclipse profiles in a bright and dim state, and many equivalents can be found at different epochs in the AAVSO data. In the right-hand panel of Fig. 2, the eclipse profile with the smallest eclipse depth is presented (which occurs when the system is brighter). The plot in the left-hand panel corresponds to one of the deepest observed eclipses during the overall decrease of the object brightness. They both were fitted with congruent models. The fit aims to determine system parameters of RW Tri, given that it is a high inclination system located at a distance of 315 pc. We also have the measure of the secondary orbital velocity $K_2 = V \sin(i) = 200$–240 km s^{-1}. In addition, we assume that a standard steady-state accretion defines the disc temperature radial profile $T \propto R^{-3/4}$ with an accretion rate of $\dot{\rm M} \approx 10^{-9} - 10^{-8}$ M$_\odot$ yr^{-1}. The last assumption is based on the previous study of the system (see Section 1), our low-resolution spectroscopy, and the object brightness.

Free parameters of the fit are the mass of the primary ($M_{\rm WD}$), the mass ratio ($q \equiv M_2/M_{\rm WD}$), the mass transfer rate ($\dot{\rm M}$), the system inclination (i), the outer radius of the accretion disc ($R_{\rm disc}^{\rm out}$), the disc height at the outer radius ($h_{\rm disc}^{\rm out}$), and the effective temperature of the secondary (T_2). The formal temperature of the primary WD was selected to be 30 000 K. It can be significantly higher because the dominating source of radiation is the inner part of the accretion disc. The variation

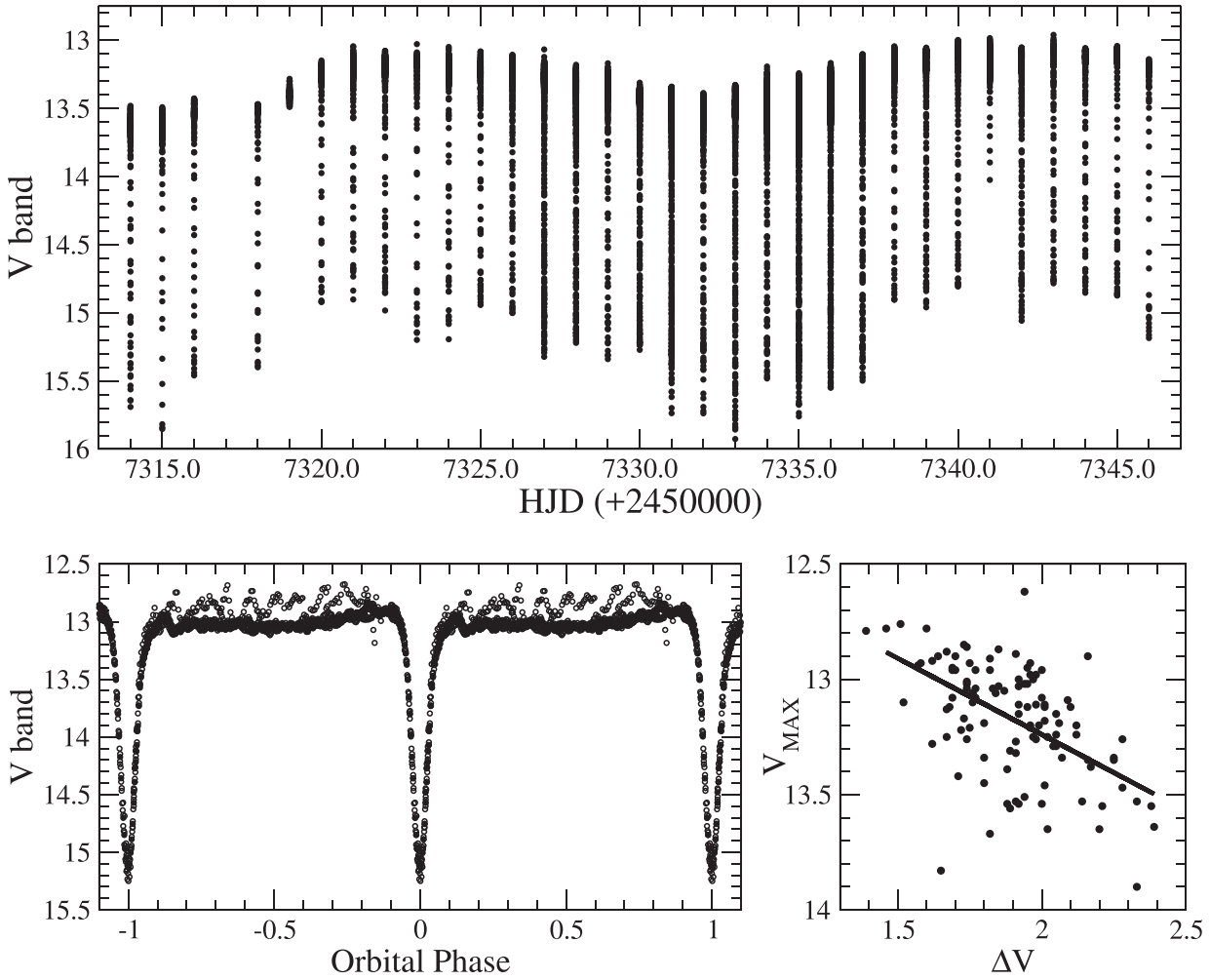

Figure 1. Top panel: Long-term light curve of RW Tri collected by AAVSO. Bottom left-hand panel: The example of the *V*-band light curve of RW Tri folded on the orbital period. The data were obtained in four consecutive nights in OAN-SPM. The light curve with flickering is shown by the open circles and the opposite is presented by the filled circles. The difference in out-eclipse behaviours for diverse orbital cycles is clearly visible. Bottom right-hand panel: The relationship between out-eclipse maximal brightness and the depth of the eclipse.

of the WD temperature in the range of 18 000 –35 000K does not affect the eclipse profile. We fixed parameters of the hotspot (length, width, and temperature) for the bright and the dim light curves to reproduce a small peak observed at the orbital phase of $\varphi \approx 0.12$.

The gradient descent method was used to find the minimum of the χ^2 function defined as

$$\chi^2 = \sum_{\rm k}^{N_{\rm k}} \left(\frac{{\rm mag}_{\rm k}^{\rm obs} - {\rm mag}_{\rm k}^{\rm calc}}{\sigma\ {\rm mag}^{\rm obs}} \right)^2, \quad (1)$$

where $N_{\rm k}$ is the number of observed points in each fitted light curve.

The values of the best-fitting model are presented in Table 3. A mosaic of square-shaped panels on the left-hand side of Fig. 2 illustrates errors of the fit attained for the deep eclipse in the dim state of brightness. The light curve in a brighter state was reproduced with the same system parameters, but with a higher value of mass transfer rate than in the dim state. The outer radius of the disc $R_{\rm disc}^{\rm out} = 0.58 R_\odot$ is close to the tidal limiting radius $R_{\rm disc}^{\rm max} = \frac{0.6}{1+q} a = 0.62 R_\odot$. It is consistent with the $R_{\rm disc}^{\rm out} = 0.53 - 0.63 R_\odot$ estimate from the NIR photometry of Longmore et al. (1981) recalculated for a new *GAIA* distance. This size of the disc provides the minimum velocity of the Keplerian disc of $\upsilon_{\rm min} \sin(i) = 470$ km s^{-1}. This velocity is shown by a circle in the Doppler maps in Fig. 7. The system inclination $i = 77\overset{\circ}{.}2 \pm 0.5$ is very well constrained and is consistent with the $77\overset{\circ}{.}5$ value deduced by Longmore et al. (1981) from the eclipse width in the NIR. The temperature at the outer radius of the disc, according to our model, is about 5000 K, and the maximum temperature of the hotspot is ∼7100 K. The inner temperature in the disc reaches up to ∼35 000 K. The deduced secondary effective temperature $T_2 = 3675(125)$ K corresponds to M1.5V spectral type. However, its radius is about 20 per cent larger than a corresponding ZAMS star. The main difference between the bright and the dim states in our model, apart from the change of the mass transfer rate, is related to the vertical width of the accretion disc at the edge. In general, all observed optical eclipse light curves can be reproduced with reasonable errors using the best-fitting values with a variation of those two parameters.

We fitted the NIR *J*- and *K*-band light curves published by Longmore et al. (1981) using our models for the dim and the bright states. We found that our model successfully reproduces observed NIR light-curve shapes. However, the calculated flux is about 0.5 magnitudes fainter than it was reported by Longmore et al. (1981).

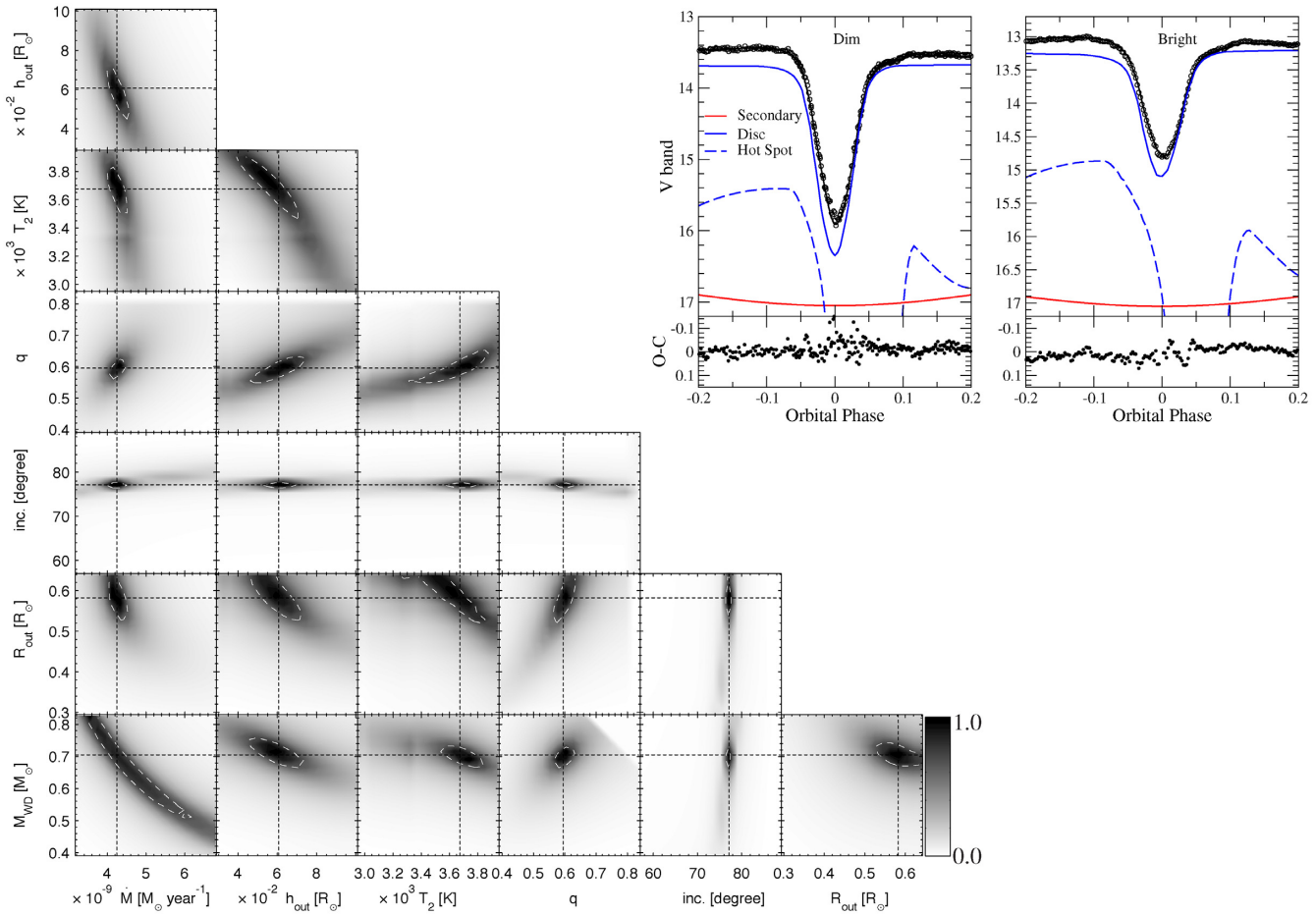

Figure 2. Top right-hand panels: Examples of eclipses (open circles) in the 'bright' (right-hand panel) and in the 'dim' (left-hand panel) state of the system and results of the light-curve modelling (solid line). Contribution of different system components in the total flux are marked. The corresponding O − C (observed minus calculated) diagrams are given in the bottom panels of this plot. Left grey scale panels: Errors of the fit for the light curve in the 'dim' state. The black dashed lines mark the best-fitting values of parameters. The white long-dashed lines corresponds 1σ errors of parameters.

Table 3. System parameters used in the light-curve modelling.

Fixed:			
$P_{\rm orb}$	20034.72 s	$E(B-V)$	0.10
Distance	315(5) pc	$V_2 \sin(i)$	221(29) km s^{-1}
Variable and their best values:			
i		77.2(5)	
$M_{\rm WD}$		0.70(3) M$_\odot$	
R_1		$0.011 R_\odot$	
q		0.60(3)	
M_2		0.42 M$_\odot$	
T_2		3675(125) K	
R_2		$0.55 R_\odot$	
$R_{\rm disc}^{\rm out}$		$0.58(4) R_\odot$	
Dim			
$\dot{M}$		$4.3(2) \times 10^{-9}$ M$_\odot$ yr^{-1}	
$h_{\rm disc}^{\rm out}$		$0.06(1) R_\odot$	
Bright			
$\dot{M}$		7.8×10^{-9} M$_\odot$ yr^{-1}	
$h_{\rm disc}^{\rm out}$		$0.10 R_\odot$	
a		$1.65 R_\odot$	
$V_1 \sin(i)$		135 km s^{-1}	

Note. Numbers in brackets throughout the paper are 1σ uncertainties referring to the last significant digits quoted.

An excess in IR fluxes for wavelengths longer than ∼3–5 μm over expected from the standard model accretion disc was noted previously by Hoard et al. (2014) for the sample of 12 NLs. Therefore, we do no exclude IR excess that may appear at a shorter wavelength range. The size and shape of the eclipse are different in the UV, optical, and IR bands. If in UV domain, the full eclipse has a U-shape and lasts $\approx 0.07 P_{\rm orb}$ (Mason et al. 1997), in optical and NIR bands, it is *V*-shaped with a full time of $\approx 0.14 P_{\rm orb}$, and $\approx 0.2 P_{\rm orb}$, respectively (Longmore et al. 1981). It is clear that the disc is larger in the IR, not exactly circular or symmetric regarding the view of sight (see e.g. Hensler 1982; Meglicki, Wickramasinghe & Bicknell 1993; Murray 1996; Kunze, Speith & Hessman 2001; Ju, Stone & Zhu 2017, and references therein). Most probably, the outer fringe of the disc is ragged and not even in a vertical extend. All these departures from the ideal models might play a role in deviations of infrared flux, detection of a dip at the orbital phase of $\varphi \sim 0.7$ in the UV light curve, and other inaccuracies compared to our and other models.

4.1 O − C diagram

Since its discovery, RW Tri has been continuously monitored, and many precise mid-eclipse epochs were determined. Thus its orbital period is known with a high precision of the order of

Table 4. Precise times of RW Tri eclipses measured in Ondřejov during 2012–2020.

HJD-2400000	Error (d)	Filter	Epoch
56527.56969	0.0001	*R*	66 405
56540.55508	0.0001	*R*	66461
56624.26501	0.0001	*R*	66 822
56659.27939	0.0001	*R*	66 973
56870.52515	0.0001	*R*	67 884
56926.40887	0.0005	*R*	68 125
57059.27813	0.0001	*R*	68 698
57295.33559	0.0001	*R*	69 716
57327.33545	0.0001	*R*	69 854
57384.37895	0.0001	*R*	70 100
57720.37804	0.0001	*R*	71 549
57722.23322	0.0001	*V*	71 557
57739.39218	0.0001	*V*	71 631
57780.20443	0.0001	*R*	71 807
57798.29077	0.0001	*R*	71 885
57958.52201	0.0001	*R*	72 576
57994.46451	0.0001	*V*	72 731
58004.43543	0.0001	*V*	72 774
58041.53636	0.0001	*V*	72 934
58089.30455	0.0001	*V*	73 140
58149.36246	0.0001	*V*	73 399
58169.30443	0.0001	*V*	73 485
58185.30428	0.0002	*V*	73 554
58326.52106	0.0002	*V*	74 163
58329.53560	0.0002	*V*	74 176
58366.40488	0.0002	*V*	74 335
58387.50619	0.0002	*V*	74 426
58429.24511	0.0001	*V*	74 606
58458.23023	0.0001	*V*	74 731
58502.28782	0.0001	*V*	74 921
58505.30230	0.0001	*V*	74 934
58506.22975	0.0001	*V*	74 938
58527.33128	0.0001	*V*	75 029
58710.51838	0.0001	*V*	75 819
58714.46076	0.0002	*V*	75 836
58773.59019	0.0001	*R*	76 091
58773.59025	0.0001	*V*	76 091
58828.31536	0.0001	*R*	76 327
58828.31551	0.0001	*V*	76 327
58866.34418	0.0001	*R*	76 491
58866.34411	0.0001	*V*	76 491
58892.31521	0.0001	*R*	76 603
58892.31517	0.0001	*V*	76 603

$\sim 10^{-3}$ s (Walker 1963; Africano et al. 1978; Robinson et al. 1991). Using high-time precision photometric data obtained in Ondřejov Observatory, we calculated the time and uncertainties of each full eclipse by the least-squares Gaussian fitting of eclipse profiles. The predicted epochs of eclipses were calculated using the ephemeris of Robinson et al. (1991):

$$T_{\rm min} = \text{HJD } 2441129.36487(10) + 0\overset{\rm d}{.}231883297(6) \cdot \text{E}. \quad (2)$$

They are given in Table 4. The search for O − C periodic variation was performed using all available mid-eclipse times found in the literature (O − C gateway[1]), including our new results.[2] A total of 221 reliable times of minimum light of different weights were gathered. The historical O − C diagram is plotted in Fig. 3, bottom panel. Obviously, mid-eclipse times do not follow a simple linear or parabolic trend. The data can be fitted roughly by a sinusoidal curve with a period of ∼41.2 yr and the semi-amplitude of 160 s. This result is consistent with the O − C behaviour recently reported by Boyd (2012). If this periodicity is real, it might be related to the presence of a third body in the system at a wide orbit. For example, the third body in a similar system, LX Ser, was recently reported by Li et al. (2017). An alternative explanation of cyclic period changes in RW Tri could be the Applegate mechanism (Applegate 1992) due to the magnetic activity of the red dwarf component. According to this mechanism, a solar-like magnetic cycle would result in shape changes causing redistribution of the angular momentum within the interior of the secondary. The change of the stellar quadrupole moment then leads to the variation of the orbital period. Our estimation of the O − C periodic variation with $P \approx 42.2$ yr is comparable with the mean value (40–50 yr) of quadrupole moment changes/modulation in magnetically active close binaries (Lanza & Rodonò 1999).

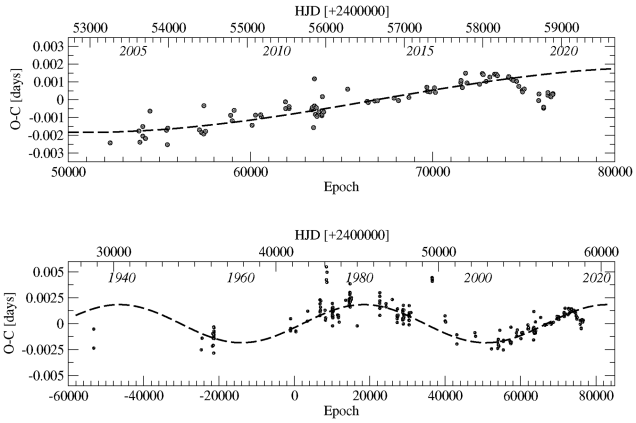

Figure 3. Bottom panel represents the historical O − C diagram for the mid-eclipse times of RW Tri. Individual minima are denoted by circles. The dashed sinusoidal curve represents a possible period (42.2 yr) present in O − C variation. At the top, the O − C diagram of the ultimate decade is presented in detail based mostly on our new measurements from Ondřejov. A rapid decrease of the orbital period since 2018 is visible.

However, the periodicity is not an established fact, and more observations are necessary to confirm its reality. A portion of $O - C$ diagram, based only on our recent precise-timing data, is plotted in the top panel of Fig. 3. Since 2018, the orbital period abruptly decreases, deviating from the sinusoidal trend marked by the dashed line.

5 SPECTROSCOPY AND DOPPLER TOMOGRAPHY

5.1 Low-resolution spectroscopy

Low-resolution spectra of RW Tri throughout eclipse and outside of it are shown in Fig. 4. In those spectra, the Balmer lines have single-peaked emission profiles, but not regular Gaussian shapes. Meanwhile, multiple He I lines in the observed range are double-peaked in contrast to the relatively strong but single-peaked He II

[1] http://var2.astro.cz/ocgate, Paschke & Brat (2006).

[2] Besides those minima included in Table 4, we used the previous collection of eclipse times obtained by Walker (1963), Warner (1973), Winkler (1977), Africano et al. (1978), Smak (1979), Robinson et al. (1991), Dmitrienko (1992), Rutten et al. (1992), Polsgrove et al. (2006), Zejda, Mikulasek & Wolf (2006), Boyd (2012), and many other amateur observers.

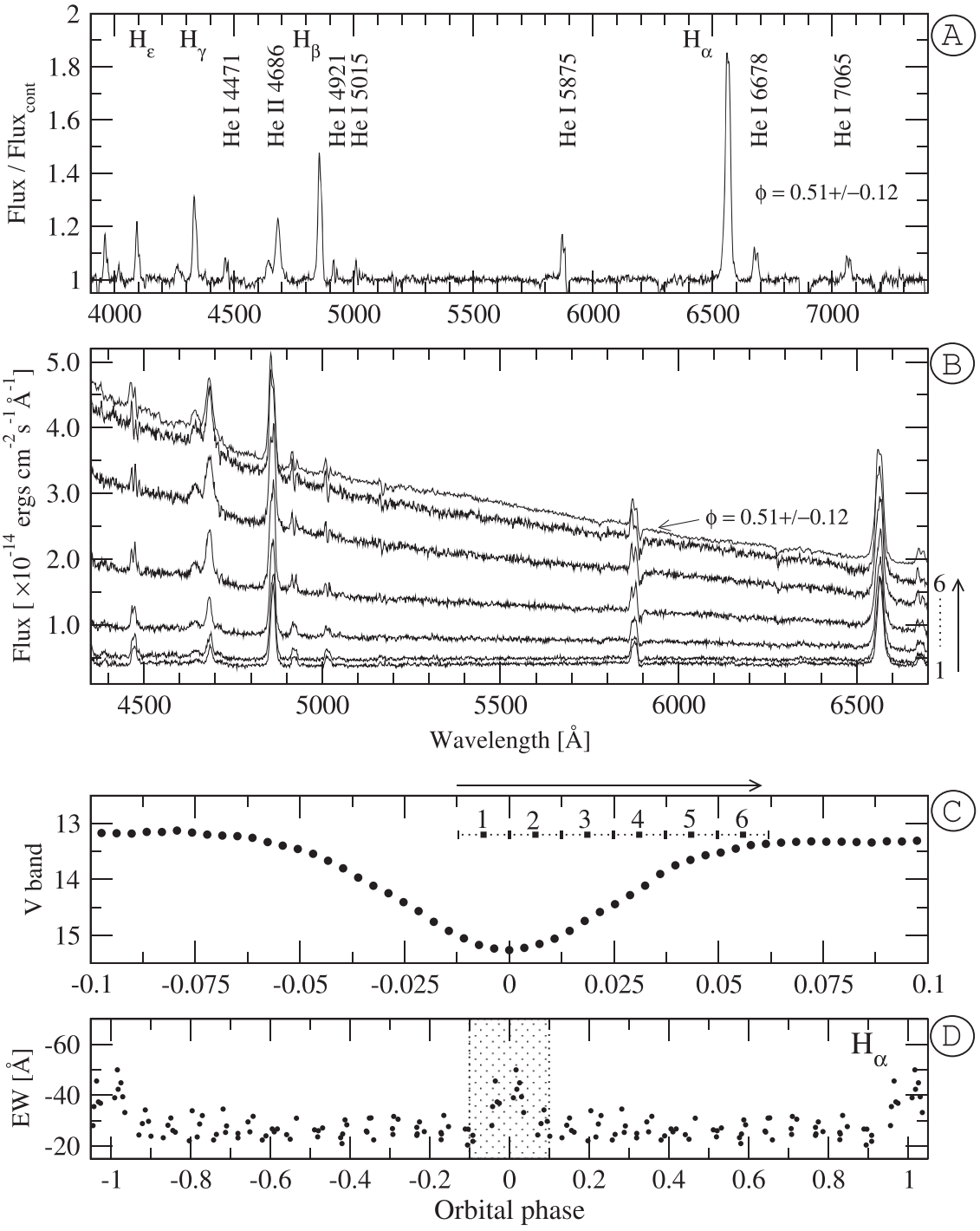

Figure 4. Panel A: normalized low-resolution spectrum of RW Tri averaged over a stretch of $\varphi = 0.47-0.73$ orbital phases. Panel B: Spectral evolution of RW Tri from the bottom to clearing of the eclipse. The final (top) spectrum corresponds to the average spectrum for $\varphi = 0.47-0.73$ orbital phases. Panel C: The eclipsing light curve of RW Tri in the *V* band obtained close to the spectral observations. The filled squares mark the orbital phases when the spectra were acquired. Panel D: The behaviour of equivalent widths (EW) of the Hα emission line during the orbital period. The selected region corresponds to the Panel C abscissa range.

λ4686Å line. There is no evidence of underlying absorption or P Cyg-like features in Balmer lines frequently observed in other NL systems. The out-of-eclipse spectrum shows a blue continuum with a slope of $\alpha \approx -2.4$ where $F \propto \lambda^{-\alpha}$, close to the standard value of -2.33 for the steady-state disc (see Fig. 4, panels A and B). The ratio of equivalent widths (EW) of Balmer lines is EW = Hα:Hβ:Hγ:Hδ:Hε = 23.97:9.22:6.74:3.36:2.56 Å. At the bottom of the eclipse, the spectrum of the source is rather flat, with its blue extreme gradually increasing towards eclipse end, as it is clearly seen from a sequence of six low-resolution spectra obtained on 2016 September 27 (see Fig. 4, panels B and C). The first two spectra correspond to the moments of minimum in the eclipse. All lines, including He I are

Table 5. The evolution of some emission-line parameters during way out of the eclipse.

Orbital phase	$I_{H\alpha}$	$EW_{H\alpha}$ Å	$I_{He\,I}$ 4471Å	$EW_{He\,I}$ Å	$I_{He\,II}$ 4686 Å	$EW_{He\,II}$ Å
0.993	1.33	− 75	0.31	− 12.4	0.28	− 9.2
0.006	1.26	− 72	0.35	− 11.0	0.31	− 10.2
0.019	1.39	− 56	0.30	− 6.4	0.52	− 10.9
0.031	1.45	− 42	0.47*	− 3.7	0.78	− 10.6
0.043	1.55	− 30	0.40*	− 1.2	0.80	− 8.6
0.056	1.65	− 27	0.39*	− 0.5	1.00	− 6.2

Notes. [a]Double-peaked. Peak intensity (I) without continuum in $\times 10^{-14}$ ergs cm^{-2} s^{-1} Å^{-1};

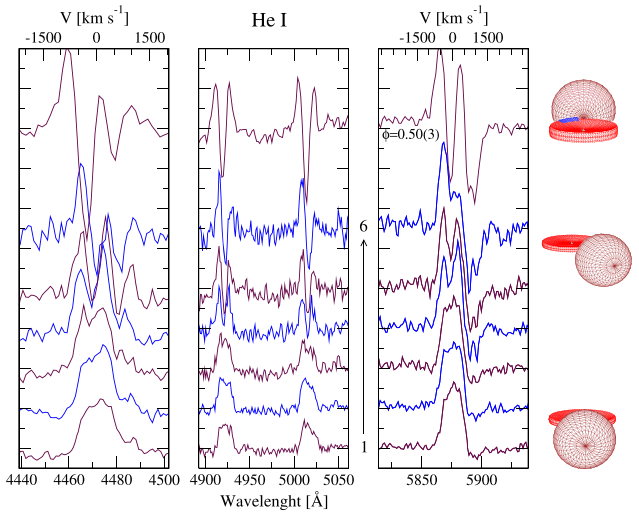

Figure 5. Evolution of He I line profiles during the eclipse (marked by 1–6) and at the orbital phase $\varphi = 0.5$. The continuum removed from the spectra after they were shifted along the y-axis for the best presentation. The right-hand side of the plot presents an artistic view on the system at its corresponding orbital phases.

single-peaked at a depth of eclipse with full width at half-maximum (FWHM) $\approx$ 800 km s^{-1}. All emission lines are visible during the deepest eclipse phase. As the inner parts of the accretion disc open up, flux grows with the slope of the continuum becoming bluer, and the intensities of emission lines start to increase, especially He II (see Table 5). The shape of the He II λ4686Å line profiles looks single peaked in all orbital phases.

Meanwhile, He I transforms into a double-peaked and the Balmer lines show complex structure. The EWs of Hα and He I decrease significantly as the system leaves the eclipse in contrast to He II λ4686Å. The evolution of $EW_{H\alpha}$ during the full orbital period is shown at the bottom panel of Fig. 4 (measured from the high-resolution Echelle spectra). It is clear that $EW_{H\alpha}$ stays constant in a range of values and only increases during the eclipse as most of the radiation from the accretion disc falls.

Especially noteworthy is the evolution of He I throughout the eclipse (see Fig. 5). It is drastically different from other lines. At the moment of the full eclipse, the line has a single peak, somewhat boxy shape centred at about zero radial velocity. As the accretion disc re-appears from behind the secondary, the line profile obtains two nearly symmetric sharp peaks. In other words, a strong absorption component appears, nearly centred relative to the emission-line (the fourth spectrum from the bottom to the top in Fig. 4, panel B, and

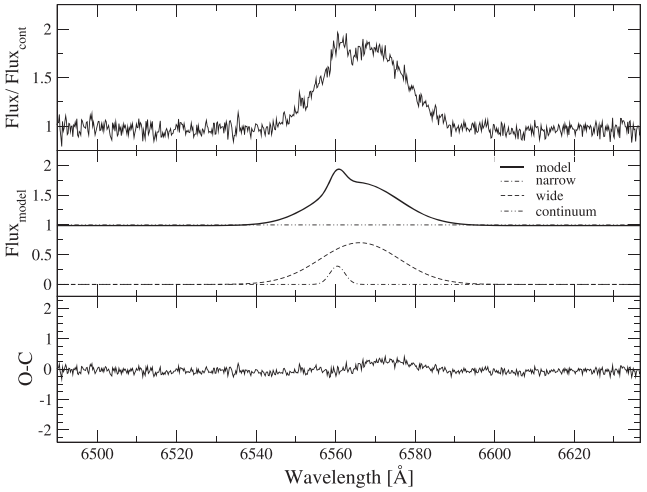

Figure 6. An example of the high-resolution Hα profile of RW Tri (top panel), the result of a double-Gaussian fit to the profile (middle panel), and the residuals between the observed and calculated profiles (bottom panel). The spectrum was normalized to the continuum.

Fig. 5). The appearance of central absorption in He I is accompanied by the emergence of Na I λ5890Å and 5896Å doublet and probably Mg II λ4481Å, all in the flanks of He I lines. We believe that the latter forms at the inflated side-wall of the disc, where the temperature is $T_{\rm disc}^{\rm out} \gtrsim 5000K$. As the disc continues revealing itself, the blue peak becomes visibly stronger while the red one nearly disappears, which is when the secondary shades solely the edge of the disc moving away from the observer. We can assume He I is emanated mostly by the edges of the disc surface, which are still visible in the middle of an eclipse. None of these profile transformations is observed in Balmer lines. We see no need to invoke a disc wind model to explain the presence of He I line in the spectrum of RW Tri at the minimum of an eclipse. At a depth of eclipse, the profile can be formed by two Gaussians from disc extremes still visible on either side of the secondary, while the central parts of the disc, where the absorption forms, are blocked. However, the situation with other emission lines is different, and they are better accessible by higher resolution spectroscopy.

5.2 High-resolution spectroscopy

The high-resolution Echelle spectra leave no doubt about the two-component structure of the Balmer emission lines (Fig. 6). The trailed spectrum of Hα (see Fig. 7, top left-hand panel) clearly shows narrow, low-velocity and wide, higher velocity components, which are approximately in anti-phase. It is very similar to what was recently reported by Hernandez et al. (2017) for two other NL systems RW Sex and 1RXS J064434.5 + 334451. Hernandez et al. (2017) used the same technique to separate two (narrow and wide) components of Hα profile (Fig. 6). In a simple rendition of components, they are Gaussians, characterized by the peak intensity I, the FWHM, and their radial velocities depend on the orbital phase of

$$\upsilon = \gamma + A\sin[2\pi(\varphi - \varphi_0)]. \quad (3)$$

The parameters of both Gaussian components of the Hα emission core are presented in Table 6.

It is obvious that the Gaussian description of components is a simplification. However, it allows us to remove the narrow Gaussian line from the Hα emission-line profile to probe the origin of both its

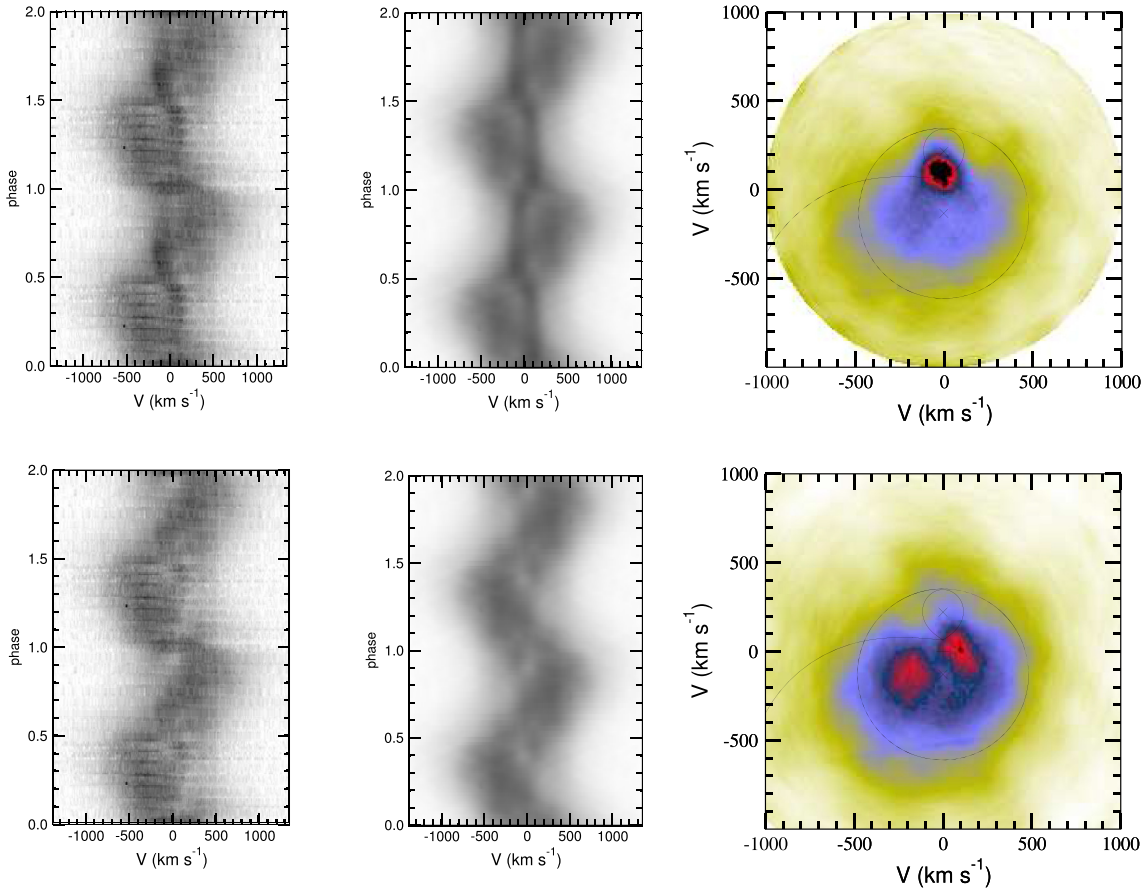

Figure 7. Top panels from the left- to the right-hand side: the observed, reconstructed trailed spectra around Hα emission line and corresponding Doppler tomogram. Bottom panel: the observed, reconstructed, and Doppler tomogram after removing the narrow component of the emission line. The Keplerian velocity of the disc in the Doppler maps is located at $\upsilon_{\rm disc}\sin(i) \geq 470$ km s^{-1} and the circle shows the disc external radius. The system parameters discussed in the text.

Table 6. Parameters of the Gaussian components of the Hα emission line.

Emission component	A$\equiv V \sin$ (i) (km s^{-1})	V (km s^{-1})	$I/I_{\rm c}$	FWHM (km s^{-1})	φ_0 (phase)
Narrow	134.8	138.3	0.35	173	0.06
Wide	300(50)	310(50)	0.71	1042	0.40

components. From the trailed spectra, we can infer that the intensity of the narrow component depends on the orbital phase. The maximum of this component intensity is located at the orbital phase of $\varphi \approx 0.6$ and decreases as the system going to the eclipse. The wide component is complex, with variable peak intensity and FWHM. As a result, its radial velocity amplitude is determined with large uncertainties.

5.3 Doppler tomography

We use the Doppler tomography technique (Marsh & Horne 1988; Marsh 2001) to probe the accretion flow structure in RW Tri. Briefly, the Doppler tomography technique uses the information encoded in spectral line profiles taken at different orbital phases to calculate a distribution of emission over the binary. Doppler tomography provides a quantitative mapping of the optically thin line forming regions in velocity space. The maximum entropy method implementation developed by Spruit (1998)[3] was used to generated Doppler maps.

The Doppler tomography of the Hα line based on Echelle spectra is presented in Fig. 7, top right-hand panel. The orbital zero-phase was determined from the photometric data (eclipses), and the secondary Roche lobe size, the accretion stream trajectory, and the maximum size of the disc were derived from the system parameters determined above. The Doppler map of the entire line, in which the narrow component is quite dominant by its intensity and concentration, brilliantly confirms the proposition that the narrow component is formed close to the face-on of the secondary nearly the L_1 point of the system. The residual trailed spectra (observed and reconstructed) after the narrow component was removed shown in Fig. 7, bottom left-hand panel, and centre panels. The corresponding Doppler tomogram is presented in Fig. 7, bottom right-hand panel. The circle in the Doppler tomogram marks the truncation radius of the disc. The residual trailed spectra (observed and reconstructed) after the narrow component was removed are shown in Fig. 7, bottom left-hand and centre panels. The corresponding Doppler tomogram is presented in Fig. 7, bottom right-hand panel. The circle in the Doppler tomogram marks the truncation radius of the disc. This map looks like a horseshoe with two bright extended regions located at ($V_x \approx -100$ km s^{-1}, $V_y \approx -200$ km s^{-1}) and ($V_x \approx 150$ km

[3]https://wwwmpa.mpa-garching.mpg.de/henk/pub/dopmap/

s^{-1}, $V_y \approx 0$ km s^{-1}). The latter is somewhat unusual. The velocity map is probably affected by artifacts created by narrow component inaccurate removal; however, this extended spot is certainly not related to the accretion disc. The wide component radial velocity and its reflection in the velocity map attest that it has a lower value than the minimal Keplerian velocity $\upsilon_{\rm min}\sin(i) = 470$ km s^{-1} in the accretion disc may have. Presumably, this component of the emission line is not formed in the accretion disc either. It is a common feature detected in high-resolution spectra of the NLs RW Sex and 1RXS J064434.5 + 334451. Similar Doppler tomograms were reported for another long period NLs such as AC Cnc and V363 Aur (Kaitchuck et al. 1994; Thoroughgood et al. 2004).

As a result of the systematic study of NLs affiliated to UX UMa or RW Sex type by high-resolution spectroscopy, we drew a consistent picture, according to which the Balmer emission lines arise from two separate sources. Doppler maps consistently reproduce a pattern very similar to Fig. 7, and it permits us to discuss a common phenomenological model for this type of CVs.

6 DISCUSSION

Among a few models invoked to explain single-peaked emission-line profiles NLs the disc wind model (Knigge, Woods & Drew 1995; Murray & Chiang 1996; Proga 2005; Noebauer et al. 2010; Matthews et al. 2015, and references therein) prevails. In a recent study, Matthews et al. (2015) explored whether the disc wind models influence NLs spectra in the UV/optical wavebands. They applied a standard disc wind model to RW Tri and found that the model successfully reproduces the UV spectra of CVs and also leaves a significant imprint on the optical spectrum. The wind can participate in the formation of the Balmer and He lines. However, in most cases, no single-peaked line is formed except the narrowing of the double-peaked emission lines. Authors also note that the slowly accelerating wind models produce narrower emission lines, and in order to generate strong optical wind signatures, very high densities ($n_{\rm e} \sim 10^{13}$–10^{14} cm^{-3}) at the base of the wind are needed. Another problem of these models is that they require considerably stronger He II features than is observed.

Our new high-resolution optical spectroscopy of the eclipsing NL system RW Tri shows a single-peaked but two-component structure of the Balmer lines and their phase-dependent behaviour similar to other NLs (e.g. RW Sex and 1RXS J064434.5 + 334451, which are populating the same orbital period range, Hernandez et al. 2017). Emission from He II is present, but it is weaker than required by the wind model. Hernandez et al. (2017) reviewed various proposed models to explain emission-line profiles in NLs and concluded that their behaviour in high-mass transfer CVs is associated with the matter escaping from the accretion disc in the orbital plane, and forming an extended low-velocity region (hereafter called an outflow zone) opposite to hotspot side of the disc. This region is a possible source of the wide component of the Balmer line profiles in RW Tri, RW Sex, and 1RXS J064434.5 + 334451, and some other long-period NLs with similar Balmer-line profiles.

A list of such NLs is presented in Table 7. We selected only systems with known orbital periods longer than ≈4 h because a significant fraction of the population of NLs in the 3–4 h period range are SW Sex systems (Rodríguez-Gil et al. 2007). In the latter, the hotspot probably plays a dominant role in the formation of emission lines (Tovmassian et al. 2014). NL-systems with longer orbital periods show distinct characteristics compared to SW Sex systems. High-resolution spectroscopy of RW Tri, BG Tri, RW Sex, 1RXS J064434.5 + 334451, AC Cnc, and V363 Aur exhibit typical two-component structure of the Balmer lines clearly illustrated by trailed spectra (see references in Table 7). Here, we put together main spectral characteristics of NLs including the presence or absence of Balmer absorptions, available radial velocities of components of the Hα emission line, evidence of spiral arms, and presence of He IIλ4686Å line or a ratio of peak intensities $I_{\rm He}/I_{\rm H\beta}$. Only low-inclination systems exhibit Balmer adsorptions. The majority of objects do not exhibit strong He II emissions, which, as we believe, could be an indication of the presence of the disc wind. In a few cases, the Doppler maps of Balmer lines were interpreted as evidence of spiral arms.

In Fig. 8, we reproduce the geometry and an observer view of the system during the eclipse and mark by arrows both regions, which are responsible for emission-line formation according to our interpretation. The system parameters of RW Tri, obtained from our optical light-curve fit, were used. The narrow, low-velocity component of Balmer emission lines forms at the heated face of the secondary because its radial velocity (138.3 km s^{-1}) is about twice larger than the orbital velocity of the L_1 point ($\upsilon_{\rm L_1} = 64.7$ km s^{-1}). Meanwhile, the radial velocity of the secondary (centre of mass) reaches 225 km s^{-1}. The intensity of the narrow component is phase-dependent, as shown in the trailed spectra (Fig. 7, top left-hand panel). The narrow component is brighter at the orbital phase $\varphi \sim 0.6$ and practically disappears around the eclipse. The fact that in NLs the disc is capable of irradiating the face of the secondary means, it also easily excites the gas in the outflow region to produce emission lines. Meanwhile, in DNe, we seldom detect emission lines from the L_1 point, because the optically thin disc can not provide sufficient energetic photons. Hence, we do not see the outflow region either. Besides, in DNe, the accretion rate is lower, and the outflow rate is undoubtedly lower.

The wide component of Balmer lines in our model corresponds to the outflow zone located in the opposite to the standard hotspot position and is always visible in all orbital phases, including the eclipse (see the top panels of Fig. 8). On average, it has a semi-amplitude of the orbital velocity of ≈300 km s^{-1}, but naturally shows large velocity dispersion since the line-forming particles have diverse velocities in the non-Keplerian outflow zone. Examples of hydrodynamic simulations detailing disc outflow in the orbital plane around this region were presented by Sytov et al. (2007), Bisikalo & Kononov (2010), Ju et al. (2017), and Kaygorodov (2019). Interestingly, this outflow region is confined to the Roche lobe of the WD, and the maximum orbital velocity of the Roche lobe extreme is also ∼300 km s^{-1}. If, in contrast, the wide component forms at the base of a disc wind, it is expected to have a radial velocity compatible with the WD, or more than twice smaller. However, the measured velocities of wide and narrow components, when it was possible to separate them clearly, show that the former's semi-amplitude is always higher (see Table 7), while in systems with $q < 1.0$ should be the opposite. The radial velocity of the wide component in all NLs after correction for the inclination angle (notwithstanding the uncertainties) is regularly around ∼300 km s^{-1}. This value is too high for a wind originating from the hot, inner parts of the accretion disc, but it is reasonable if the wide component formation area is located in the orbital plane beyond the disc.

However, most models of the outflow of matter from accretion discs are associated with possible wind from the accretion disc. We agree that the wind exists because it allows us to explain common characteristics of the velocity field produced by emission lines in a group of similar objects in the UV. Nonetheless, in high-mass transfer systems with thick accretion discs, the impact of the mass transfer

Table 7. List of NLs ($P_{\rm orb} \gtrapprox 4$ h) and their principal characteristics.

Object	Orbital period (d)	Dist. (ps)	G band (mag)	Incl. angle (°)	Absence/presence	Narrow km s^{-1} $V_{\rm obs}/V$	Wide km s^{-1} $V_{\rm obs}/V$	Spiral arms[a] comp. presence	He II/Hβ[b] $I_{\rm He}/I_{\rm H\beta}$	Reference
EC21178-5417	0.15452	537(9)	13.73	83(7)	N	–	–	Y	2.0	1
LX Ser	0.1584	492(10)	14.96	75(2)	N	–	–	–	0.6	2
BG Tri	0.15845	337(8)	11.87	21(3)	Y	78/180	121/300	N	Weak	3
HS 0139 + 0559	0.16920	1304(102)	15.07	n. ecl.	Y	–	–	–	N	4
IPHAS J210205 + 471018	0.1776	740(20)	15.49	n. ecl.	Y	175[c]	–	–	Weak	5
SDSS 1006 + 23	0.18591	796(60)	18.25	81.3(8)	N	–	–	Y	0.5	6
IX Vel	0.19293	90.5(2)	9.32	57(2)	Y	–	–	Y	0.7	7
UX UMa	0.19667	297(2)	12.98	71	N	–	–	–	0.2	8
V345 Pav	0.19810		13.39	ecl.	N	–	–	–	0.9	9
V825 Her	0.20600	1078(30)	14.12	n. ecl.	Y	–	–	–	–	10
V3885 Sgr	0.20714	132(1)	10.25	n.ec.	Y	-	–	Y	1.6	11
2MASS 2256 + 59	0.22860	494(5)	14.53	78.8(1)	N	–	–	–	–	12
V347 Pup	0.23119	296(1)	13.42	84.0(2.3)	N	–	–	N	0.5	13
RW Tri	0.23188	315(5)	13.35	77.2(5)	N	132/136	300/310	N	0.5	14
DO Leo	0.23452	1463(117)	16.85	ecl.	N	–	–	–	0.2	15
RW Sex	0.24507	230(5)	10.63	34(6)	Y	50/90	165/294	N	Weak	16
CM Phe	0.26890	315(4)	15.49	w. ecl.	N	–	–	–	–	17
RXJ 0644 + 33	0.26937	476(7)	13.39	74(3)	N	69/71	297/309	N	1.0	16,18
AC Cnc	0.30048	673(27)	14.26	76.3	N	Y	Y	N	0.3	19
V363 Aur	0.32124	486(5)	14.13	70(2)	N	Y	Y	N	1.3	19

References. (1) Ruiz-Carmona et al. (2020) and Khangale et al. (2020); (2) Young, Schneider & Shectman (1981); (3) Hernandez al. (in preparation); (4) Aungwerojwit et al. (2005); (5) Guerrero et al. (2018) (6) Southworth et al. (2009); (7) Wargau et al. (1983) and Linnell et al. (2007); (8) Neustroev et al. (2011); (9) Buckley et al. (1992); (10) Ringwald, Chase & Reynolds (2005); (11) Haug & Drechsel (1985) and Hartley et al. (2005); (12) Kjurkchieva et al. (2015); (13) Thoroughgood et al. (2005); (14) this paper; (15) Abbott et al. (1990); (16) Hernandez et al. (2017); (17) Hoard & Wachter (1998) and Woudt & Warner (2002); (18) Hernández Santisteban et al. (2017); and (19) Thoroughgood et al. (2004). n. ecl. is the absent of eclipse in the light curve; w. ecl. is the low amplitude eclipse is presented; '–' is the absent the data; 'Y' is the presence of characteristic; 'N' is the absent of characteristic; 'weak' is the weak He II λ4868Å in a spectrum with Balmer adsorptions.

[a]Spiral arm model is proposed in cited references.

[b]I = $I_{\rm peak} - I_{\rm continuum}$ – rough estimation from published spectra. [c]Obtained from a limited, median resolution data.

stream with the disc creates some specific conditions different from CVs with thin discs. Observations of NLs in UV-domain (Mason et al. 1997) show a significant dip of the UV flux prior to the eclipse. In the case of RW Tri, this dip is centred at the orbital phase $\varphi \approx 0.7-0.8$, or when the binary is viewed from the side. At this particular angle, neither the hotspot nor the outflow zone, as we identify it in Fig. 8, is directly blocking the inner disc to produce a dip. However, an alternative solution for the dip is predicted in the calculation of Sytov et al. (2007, see fig. 6 therein). The ejected material through the L_3 Lagrangian point (coinciding with the outflow region in our model) spreads further and can absorb the observed light curve, significantly stronger in UV than in other domains. We consider this notion as an additional argument in support of the idea that the outflow zone exists.

7 CONCLUSIONS

We conducted low- and high-resolution spectroscopy of the eclipsing NL system RW Tri. We also obtained photometric observations of the object as well as gathered all available AAVSO data together with data from the literature. Using our specialized code developed to model light curves of binary systems along with precise GAIA distance based on the system's spectral and photometric characteristics, we deduced parameters of the object and their uncertainties. We consider that our estimates improve similar evaluations in the past.

The more important outcome of our study addresses the problem related to the structure and the origin of emission lines. RW Tri is an exemplar of NLs in which two components of Balmer emission lines are clearly separated (see Table 7). While the origin of the narrow component easily discernible, the other component is still very much debatable. Hernandez et al. (2017) proposed the accretion disc spills out at the opposed to the secondary side. We argue that this dominant component of Balmer emission lines is produced by the gas outflow zone marked in Fig. 8. This outflow zone is not eclipsed by the secondary, has the right orbital velocity, and a large dispersion in the emitting particle velocities. It probably forms a material escaping the system through L_3 vicinity and which is responsible for some observed phenomenons in the system. We believe that the disc has sufficient flux to ignite emission lines from the outflow zone and from the secondary star surface adjacent to the L_1 point.

We do not question the existence of accretion disc wind and its presence in RW Tri; however, the wind does no form any significant emission in optical hydrogen or helium lines. The wind affects the formation of the UV spectrum of the system, but the wind models need unrealistically high densities and intense high-energy fluxes to create single-peaked emission lines in the optical domain. Another problem of the wind models is the Balmer lines' two-component structure and a relatively high orbital velocity of its wide component Also, wind models predict the strong He II λ4686Å line, similar to that observed, for example, in V Sge-type stars (Steiner & Diaz 1998). Meanwhile, He II is often weak or almost non-existent in a number of NLs (see Table 7).

We consider SW Sex-type stars ($3 \lesssim P_{\rm orb} \lesssim 4$ h) as an evolutionary descendant of NLs discussed here. A shrinking orbit results in some qualitative changes in density/temperature of the hotspot, converting it into a dominant source of emission lines, while the irradiation of the secondary and outflow region lose their significance. We should also point out that the outflow zone does not disappear, but it becomes a source of absorption features instead (Tovmassian et al. 2014). Long-period NLs are few and poorly studied, the number of bright sources available for the high-resolution spectroscopy with small-size telescopes ($\lesssim$2 m) is limited. We believe that future high-resolution spectroscopy at larger telescopes will confirm our suggestion about the origin of the emission-line components and the general idea of the similarity of accretion flow structure.

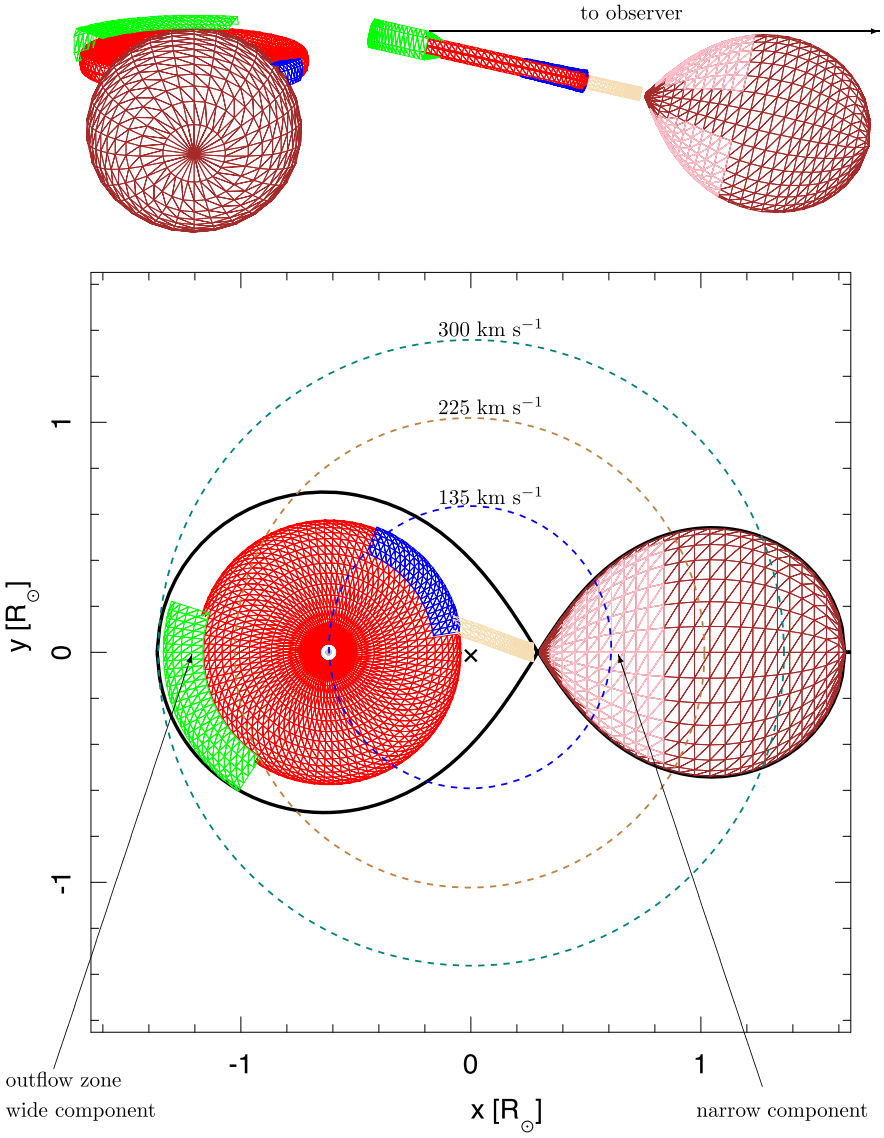

Figure 8. Bottom panel: The geometry of RW Tri. The dashed circles mark orbits of the primary, the secondary, and the disc overflowing regions. The corresponding velocities in km s^{-1} are given. The cross is the centre of mass of the system. The scale of axes is given in the solar radius. Top panel: An observer view on the system in the eclipse in the face and in the profile.

ACKNOWLEDGEMENTS

This work is based upon observations carried out at the OAN SPM, Baja California, México. SZ and GT acknowledge PAPIIT grants IN108316, IN102120, IN110619 and CONACyT grant 166376. SZ and VN acknowledge the financial support from the visitor and mobility program of the Finnish Centre for Astronomy with ESO (FINCA), funded by the Academy of Finland grant no 306531. M-SH acknowledges the Fellowship for National PhD from ANID, grant number 21170070. The research of MW was supported by the project Progress Q47 Physics of the Charles University in Prague. We acknowledge with thanks the variable star observations from the AAVSO International Database contributed by observers worldwide and used in this research. We thank the daytime and night support staff at the OAN-SPM for facilitating and helping obtain our observations. We are grateful to the anonymous referee for the useful valuable suggestions that allowed us to improve the manuscript.

DATA AVAILABILITY

The data underlying this paper will be shared on reasonable request to the corresponding author.

REFERENCES

Abbott T. M. C., Shafter A. W., Wood J. H., Tomaney A. B., Haswell C. A., 1990, PASP, 102, 558
Africano J. L., Nather R. E., Patterson J., Robinson E. L., Warner B., 1978, PASP, 90, 568
Applegate J. H., 1992, ApJ, 385, 621
Aungwerojwit A. et al., 2005, A&A, 443, 995
Bisikalo D. V., Kononov D. A., 2010, Mem. Soc. Astron. Itali, 81, 187
Boyd D., 2012, J. Am. Assoc. Var. Star Obs., 40, 295
Buckley D. A. H., O'Donoghue D., Kilkenny D., Stobie R. S., Remillard R. A., 1992, MNRAS, 258, 285
Claret A., Hauschildt P. H., Witte S., 2012, A&A, 546, A14

Dhillon V. S., Marsh T. R., Jones D. H. P., 1997, MNRAS, 291, 694
Dhillon V. S., Littlefair S. P., Howell S. B., Ciardi D. R., Harrop-Allin M. K., Marsh T. R., 2000, MNRAS, 314, 826
Dmitrienko E. S., 1992, Bull. Crimean Astrophy. Obs., 86, 58
Frank J., King A. R., 1981, MNRAS, 195, 227
Guerrero M. A. et al., 2018, ApJ, 857, 80
Hartley L. E., Murray J. R., Drew J. E., Long K. S., 2005, MNRAS, 363, 285
Haug K., Drechsel H., 1985, A&A, 151, 157
Hellier C., Robinson E. L., 1994, ApJ, 431, L107
Hensler G., 1982, A&A, 114, 319
Hernández Santisteban J. V., Echevarría J., Michel R., Costero R., 2017, MNRAS, 464, 104
Hernandez M. S., Zharikov S., Neustroev V., Tovmassian G., 2017, MNRAS, 470, 1960
Hoard D. W. et al., 2014, ApJ, 786, 68
Hoard D. W., Wachter S., 1998, PASP, 110, 906
Honeycutt R. K., Schlegel E. M., Kaitchuck R. H., 1986, ApJ, 302, 388
Horne K., Stiening R. F., 1985, MNRAS, 216, 933
Horne K., Lanning H. H., Gomer R. H., 1982, ApJ, 252, 681
Ju W., Stone J. M., Zhu Z., 2017, ApJ, 841, 29
Kaitchuck R. H., Honeycutt R. K., Schlegel E. M., 1983, ApJ, 267, 239
Kaitchuck R. H., Schlegel E. M., Honeycutt R. K., Horne K., Marsh T. R., White J. C. I., Mansperger C. S., 1994, ApJS, 93, 519
Kaygorodov P. V., 2019, INASAN Sci. Rep., 3, 225
Khangale Z. N., Woudt P. A., Potter S. B., Warner B., Kilkenny D., van der Heyden K., 2020, MNRAS, 495, 637
Kjurkchieva D., Khruzina T., Dimitrov D., Groebel R., Ibryamov S., Nikolov G., 2015, A&A, 584, A40
Knigge C., Woods J. A., Drew J. E., 1995, MNRAS, 273, 225
Kunze S., Speith R., Hessman F. V., 2001, MNRAS, 322, 499
Lanza A. F., Rodonò M., 1999, A&A, 349, 887
Levine S., Chakarabarty D., 1995, IA-UNAM Technical Report MU-94-04
Li K. et al., 2017, PASJ, 69, 28
Lin D. N. C., Williams R. E., Stover R. J., 1988, ApJ, 327, 234
Linnell A. P., Godon P., Hubeny I., Sion E. M., Szkody P., 2007, ApJ, 662, 1204
Longmore A. J., Lee T. J., Allen D. A., Adams D. J., 1981, MNRAS, 195, 825
Luri X. et al., 2018, A&A, 616, A9
McArthur B. E. et al., 1999, ApJ, 520, L59
Marsh T. R., 2001, in Boffin H. M. J., Steeghs D., Cuypers J., eds., Lecture Notes in Physics, Vol. 573, Doppler Tomography. Springer-Verlag, Berlin, p. 1
Marsh T. R., Horne K., 1988, MNRAS, 235, 269
Mason K. O., Drew J. E., Knigge C., 1997, MNRAS, 290, L23
Matthews J. H., Knigge C., Long K. S., Sim S. A., Higginbottom N., 2015, MNRAS, 450, 3331
Mauche C. W., Raymond J. C., Buckley D. A. H., Mouchet M., Bonnell J., Sullivan D. J., Bonnet-Bidaud J.-M., Bunk W. H., 1994, ApJ, 424, 347
Meglicki Z., Wickramasinghe D., Bicknell G. V., 1993, MNRAS, 264, 691
Murray J. R., 1996, MNRAS, 279, 402
Murray N., Chiang J., 1996, Nature, 382, 789
Neustroev V. V., Suleimanov V. F., Borisov N. V., Belyakov K. V., Shearer A., 2011, MNRAS, 410, 963
Noebauer U. M., Long K. S., Sim S. A., Knigge C., 2010, ApJ, 719, 1932
Paschke A., Brat L., 2006, Open Eur. J. Var. Star, 23, 13
Pecaut M. J., Mamajek E. E., 2013, ApJS, 208, 9
Polsgrove D. E., Wetterer C. J., Bloomer R. H., Newton J. D., 2006, Inf. Bull. Var. Stars, 5710, 1
Poole T., Mason K. O., Ramsay G., Drew J. E., Smith R. C., 2003, MNRAS, 340, 499
Proga D., 2005, in Hameury J.-M., Lasota J. -P., eds., ASP Conf. Ser. Vol. 330, Theory of Outflows in Cataclysmic Variables. Astron. Soc. Pac., San Francisco, p. 103
Protitch M., 1938, Astron. Nachr., 266, 95
Puebla R. E., Diaz M. P., Hillier D. J., Hubeny I., 2011, ApJ, 736, 17
Ringwald F. A., Chase D. W., Reynolds D. S., 2005, PASP, 117, 1223
Robinson E. L., Shetrone M. D., Africano J. L., 1991, AJ, 102, 1176
Rodríguez-Gil P. et al., 2007, MNRAS, 377, 1747
Ruiz-Carmona R., Khangale Z. N., Woudt P. A., Groot P. J., 2020, MNRAS, 491, 344
Rutten R. G. M., Dhillon V. S., 1992, A&A, 253, 139
Rutten R. G. M., van Paradijs J., Tinbergen J., 1992, A&A, 260, 213
Smak J., 1979, AcA, 29, 469
Smak J., 1995, AcA, 45, 259
Smak J., 2019, AcA, 69, 79
Southworth J., Hickman R. D. G., Marsh T. R., Rebassa-Mansergas A., Gänsicke B. T., Copperwheat C. M., Rodríguez-Gil P., 2009, A&A, 507, 929
Spruit H. C., 1998, preprint (astro–ph/9806141)
Steiner J. E., Diaz M. P., 1998, PASP, 110, 276
Still M. D., Dhillon V. S., Jones D. H. P., 1995, MNRAS, 273, 849
Sytov A. Y., Kaigorodov P. V., Bisikalo D. V., Kuznetsov O. A., Boyarchuk A. A., 2007, Astron. Rep., 51, 836
Thoroughgood T. D. et al., 2005, MNRAS, 357, 881
Thoroughgood T. D., Dhillon V. S., Watson C. A., Buckley D. A. H., Steeghs D., Stevenson M. J., 2004, MNRAS, 353, 1135
Tovmassian G., Stephania Hernandez M., González-Buitrago D., Zharikov S., García-Díaz M. T., 2014, AJ, 147, 68
Walker M. F., 1963, ApJ, 137, 485
Wargau W., Drechsel H., Rahe J., Bruch A., 1983, MNRAS, 204, 35P
Warner B., 1973, Inf. Bull. Var. Stars, 852, 1
Warner B., 1995, Ap&SS, 226, 187
Williams R. E., 1989, AJ, 97, 1752
Winkler L., 1977, AJ, 82, 1008
Woudt P. A., Warner B., 2002, MNRAS, 335, 44
Young P., Schneider D. P., Shectman S. A., 1981, ApJ, 244, 259
Zejda M., Mikulasek Z., Wolf M., 2006, Inf. Bull. Var. Stars, 5741, 1
Zharikov S., Tovmassian G., Aviles A., Michel R., Gonzalez-Buitrago D., García-Díaz M. T., 2013, A&A, 549, A77

This paper has been typeset from a TEX/LATEX file prepared by the author.